Earth tides can reactivate shallow faults and trigger seabed methane emissions.

N. Sultan[1*], V. Riboulot[1], S. Dupré[1], S. Garziglia[1], S. Ker[1]
[1] Geo-Ocean UMR6538, Ifremer, 29280 Plouzané, France

* Corresponding author

N.S.: nabil.sultan@ifremer.fr
V.R. : vincent.riboulot@ifremer.fr
S.D. : stephanie.dupre@ifremer.fr
S.G.: sebastien.garziglia@ifremer.fr
S.K. : Stephan.ker@ifremer.fr

Abstract

The role of solid Earth tide in fault reactivation has significant implications for understanding earthquake triggering, carbon sequestration, and the global carbon budget. Despite extensive research on this topic over the years, the relationship between Earth tide and fault reactivation remains unclear. In this study, we investigate the potential influence of solid Earth tide on the reactivation of sub-seabed fractures and faults, which may lead to the release of methane from the seabed. For a period of two weeks, we monitored the sub-seabed temperature and pore-fluid pressure at two sites on an over-pressured fault system located in the Black Sea. Our observations revealed that, despite the ~790 m distance between the two sites, the response in terms of methane discharge was synchronous during the measurement period. Our analysis showed that the presence of over-pressured fluid promotes fault reactivation under solid Earth tide cycles, resulting in synchronized degassing events. We also showed that that these faults can be reactivated with relatively low stresses, no greater than 2 kPa, illustrating the fragile equilibrium of these greenhouse gas laden systems.

Introduction

Solid Earth Tide (SET) is a global phenomenon that may influence the water level in wells (Elkhoury et al., 2006), control and modulate volcano activities (Dzurisin, 1980) and geyser eruptions (Hurwitz et al., 2014). It is however, less obvious which role the SET may mechanically play on existing fractures and faults. Several studies have analyzed the correlation between SETs and fault reactivation causing earthquakes, leading to contradictory results (Beeler and Lockner, 2003; Cochran et al., 2004; Heaton, 1982; Ide et al., 2016). Faults and fractures are the main paths for fluid migration and therefore the sensitivity of these preferential paths to the SET can promotes and modulates seabed CH_4 emissions a greenhouse gas with high-global-warming potential (Holmes et al., 2008).

In this study, we analyze the impact of SET on seabed methane (CH_4) emissions. Two sites widely investigated in the Black Sea (Ker et al., 2019; Riedel et al., 2020) with different degrees of gas hydrate (GH) accumulation affected by the presence of shallow faults were monitored using sub-seabed pore-pressure and temperature sensors. Our objective is to determine if SET cycles affect CH_4 emissions.

Results

On the Romanian margin, between 680 and 850 m water depth (Fig. 1A), the ~N-S crests, subsequently referred to as Hydrate-Ridge Crests (HRC), is a relief with an average height of 40 m. The HRC is within the GH stability zone (GHSZ), as evidenced by recent cartography of the bottom-simulating reflector (BSR) and by recovered GH cores (Riboulot et al., 2018; Riedel et al., 2021) (Fig. 1B). Along the Romanian margin, GH shallower than 750 mbsl are undergoing dissociation due to salt diffusion through the sediment (Riboulot et al., 2018) which partly explains the occurrence of gas flares in the water column (Fig. 1A). Outside the HRC area, the GH accumulations close to the base of the GHSZ, prevent gas from reaching the seafloor (Fig. 1A). At the position of the HRC and in its vicinity, inside the GHSZ, large gas flares rise from the seafloor (Riboulot et al., 2017).

The sedimentary column below the HRC is characterized by different seismic facies with a low to high-amplitude subparallel seismic reflectors related to hemipelagic layers (Fig. 2A). Transparent seismic facies with very few internal reflectors (transparent green in Fig. 2A) is related to a free gas front hampering acoustic wave propagation. Chaotic seismic facies with high-amplitude reflectors is related to the presence of GHs and possibly to the co-existence of free gas and GH. Two distinct reflectors (thick orange lines) in Fig. 2 correspond to the boundaries between clay and coarser grain layers. Below the HRC, a fault system shifts subparallel layers and affects the sedimentary column providing migration pathways to the free gas through the GHSZ (Ker et al., 2019).

Free-gas and GH in the GHSZ

Acoustic data from water column indicate that gas emissions are persistent through time in the GHSZ (Fig. 1B) with a spatio-temporal variability of gas emissions on different time scales.

In-situ piezocone soundings (CPTu) along the HRC and coring (Gas-CS14) show the occurrence of GH in the first meters of sediment (blue stratigraphic profiles in Fig. 2B). The coexistence of free-gas and gas-hydrate was detected thanks to in-situ P-wave velocity (Vp) measurements acquired from both monitoring sites: at PZG2-05 and PZG2-06, the coexistence occurs respectively below 18 mbsf and at several intervals in the first meters (fig. S1b). The visual observations from submersible dives on the seafloor along the main HRC confirm the coexistence of free gas and GH (Riboulot et al., 2021). Dives reveal the occurrence of massive-GH outcrops and meter-scale fractures and cracks associated with gas-bubble emissions (Fig. 2C).

In-situ pore fluid pressures and temperatures

Two piezometers were deployed for a two-week period on two selected segments of the HRC (Fig. 1). The PZG2-05 and PZG2-06 water depths are 818 m and 732 m respectively. PZG2-06, is located along the main HRC inside the surficial hydrate deposits (Fig. 2A). The PZG2-05 piezometer was deployed along the second less extensive fault where CPTu data (fig. S1) reveal the presence of GHs at around 24 mbsf inside a chaotic seismic facies. The top of this seismic facies is located around 15-16 mbsf.

Excess pore pressure (Δu) and temperature data are shown in Fig. 3. Continuous seabed temperature measurements show a quasi-stable value at both sites eliminating the role of a surface disturbance during the monitoring period (Fig. 3). The pressure and temperature peaks and subsequent decay periods recorded immediately after the installation are caused by the piezometer penetration. For Δu sensors, behavior differs drastically between the two sites: more than four days were needed for the pressure sensors to reach equilibrium at PZG2-05 while less than one day was needed for the Δu decay at PZG2-06. The high Δu recorded during piezometer installation is a function of the stiffness of the sediment (Burns and Mayne, 2002). The very high Δu values recorded by the two deepest sensors at PZG2-06 confirm the occurrence of GH at a shallow depth.

At PZG2-05, the temperatures at the deepest five sensors were almost constant throughout the monitoring period whilst the uppermost two sensors recorded an important deviation towards warmer temperatures (Fig. 3A). Δu data from the seven pressure sensors fluctuated throughout the monitoring period (Fig. 3). Negative Δu as low as -280 kPa were measured by the shallowest sensor. At PZG2-06, only the temperature at 3.19 mbsf was almost constant throughout the monitoring period (Fig. 3B). The uppermost three sensors recorded an important deviation towards warmer temperatures. Δu data from the four pressure sensors fluctuated modestly when compared to PZG2-05 (Fig. 3B). Negative Δu (pressure lower than hydrostatic pressure) is an indicator of upward gas emissions (Sultan et al., 2020).

The thermal gradients at PZG2-05 and PZG2-06 are determined from the sensors within the gray areas in Fig. 3 and are 31.4 and 52.5°/km, respectively (Fig. S2 and Fig. S3). In Fig. 3B, the temperature data from PZG2-05 recorded at 2.34 mbsf was superimposed on the temperature data from PZG2-06. Fig. 3C indicates the occurrence of at least five different concomitant events (numbered from 1 to 5). The duration of events varies between 12 and 24 hours, which at first glance may suggest a tidal effect on these fluctuations.

Tidal cycles

Ocean tide and SET were calculated during the monitoring period using the EarthTide-package (Kennel et al., 2021). The NS displacement of the SET was calculated for the five-month period preceding piezometer deployment indicating that a period of around 135 days separates the peak recorded during piezometer deployment from a previous comparable peak (Fig. S4).

Discussion

Synchronicity between SET and fluid activities

PZG2-05 sensors recorded on 5 September 2021 the start of small temperature perturbations (Fig. 3A) followed by negative Δu values indicating upward gas emissions. The main gas emission episode occurred between the 8 and 11 September 2021. This corresponds to an important decrease in Δu and a general trend of increasing temperature. The main degassing slowed down on 11 September 2021. Results in Fig. 3D and 3E suggest a possible interaction and concomitance between the main degassing event and the SW component of the SET.

Fig. 4A shows the SET normal (σ_n) and shear stresses (τ_n) for the fault underlying PZG2-05 with a superimposed Δu negative envelope from PZG2-05. Comparison of the synchronicity between σ_n and τ_n reveals that this evolves strongly during four different periods reaching a phase shift of almost 180° during period 4. In Fig. 4B are plotted σ_n and τ_n for PZG2-05 in three different Griffith–Coulomb diagrams corresponding to the four periods. An arbitrary tangential envelope of failure using Griffith-Coulomb criteria (Brace, 1960) was added to the diagrams. Fig. 4B demonstrates that the stress path touches the Griffith locus under extension mainly in periods 2 and 3. The Griffith locus was positioned with respect to an unknown in-situ stress state but the presence of seabed fractures (dives in Fig. 2C) suggests the occurrence of pure tensile failure during degassing events. Since the pure tensile failure occurs in the positive normal stress region (Woodcock et al., 2007), we argue that the reservoir holds an excess pore pressure equal to or higher than the lithostatic stress and that the initial effective stress in the reservoir is expected to be near zero. Therefore, excess stress (normal and shear) between 1 to 2 kPa generated by the SET could trigger the release of a highly over-pressured fluid thus feeding all overlying fractures and preferential paths. The small change in stress caused by SET between periods 2 and 3 and period 4 shows that the GH system is very sensitive to external perturbations. The synchronicity between shear and normal stresses seems to strongly affect fluid emissions (Fig. 4B). Temperature versus Δu data acquired by PZG2-05 (sensor at 2.34 mbsf) are plotted for the four different periods in three different diagrams in Fig. 4C. The data indicate an acceleration in temperature increase and in Δu decrease (degassing) when the stress path touches the Griffith failure envelope during periods 2 and 3. For period 4, the negative Δu and high temperature probably correspond to residual values and data indicate a re-equilibrium with time. The Griffith-Coulomb diagrams for PZG2-06 confirm the behavior previously observed for PZG2-05 and demonstrate a synchronicity between the two measurement sites (Fig. S7).

SET promoting methane emissions

The two normal faults (Fig. S1) provide migration pathways for over-pressured fluids. The presence of superficial coarse sedimentary layers (Fig. 2B) play an important role in the storage of free gas. The rapid expulsion of gas through existing faults and fractures can isolate free gas from the surrounding seawater by forming a hydrate covering in the GHSZ (Sultan et al., 2014). The measured in-situ temperature confirms this hypothesis. At site PZG2-05, the temperature peaks reaching 9.33°C indicate that the source of the expulsed fluid originates from 12.4 mbsf while for site PZG2-06 the temperature peaks reach 9.31°C suggesting a fluid source from 11.0 mbsf. For an average sediment unit weight of 6 kN/m^3 (Ballas et al., 2018), fluid pressure within the intermediate reservoir (between 11 and 13 mbsf) is expected to reach 66 and 78 kPa to induce gas discharge. Fluid pressure from the main gas reservoir underlying the BSR may be much higher (> 1600 kPa for an average sediment unit weight of 8 kN/m^3 (Riedel et al., 2020)) and it is very likely that degassing was initiated at this level and that the deep fluid (below the BSR) has expelled the intermediate reservoir fluid to the surface. The lack of detailed seismic imaging in the free-gas/GH coexistence zone (chaotic facies in Fig. 2 and Fig. S1) prevents defining the complex geometry of the shallow plumbing network. The evidence for this complexity lies in the piezometric data, which demonstrate the presence of lateral preferential fluid flow paths as already described for comparable structures (Sultan et al., 2016). Indeed, the deepest sensor of PZG2-06 was not affected by degassing and only the two shallowest sensors at PZG2-05 recorded degassing phases (Fig. 3). The synchronous response of the two piezometers (Fig. 3), despite the distance of ~790 m between the two sites suggests a common deep source feeding both sites.

The triggering of degassing was shown to be mainly the SW component of the SET (Fig. 3). A modest increase in stress seems able to trigger the on/off free gas release by generating pure tensile failure along the normal faults connecting the free-gas reservoir below the BSR to the shallow subsurface. Our date show that this tensile failure generated by an excess shear and normal stresses of 1 to 2 kPa is able to connect the over-pressured deep reservoir (> 1600 kPa) below the BSR to neighboring segments of the fault network and has therefore the capacity to induce the advection of highly over-pressured fluids up to the free-gas/GH complex system. Positive excess pore-pressure data measured by both piezometers (around 50 kPa at PZG2-05 and 20 kPa at PZG2-06 – Fig. 3) is strong evidence of the occurrence of such fluid advection intersecting the degassing episodes.

Implications

Marine CH_4 seeps are the seabed expression of over-pressured geological formations (Judd, 2003) and are often the consequence of overpressure release following hydrofracturing (Crutchley et al., 2013) and tensile failures (Konno et al., 2016). Methane seepage activities are often modulated through on/off sequences (Sultan et al., 2020) or alternatively through a variability of seep intensities (Marcon et al., 2022). Plausibly, the small stress generated by the SET should not significantly affect the variability of already active seeps. For the on/off mechanism, the instantaneous shut-in pressure (=leakage off) is may closely match the fracture re-opening pressure (=leakage on) when considering multiple cycles of leakage (Sano et al., 2005). In this case, it is the effect of the SET on degassing that is expected to be the most pronounced. An applied low tensile stress can make the shift between shut-in pressure and re-opening pressure. The consequence is reactivation of the gas seepage where the burst duration is controlled by the gas source internal pressure and the available quantity of gas.

The very-low-stress perturbations generated by the SET are unlikely to reactivate faults promoting earthquakes. However, as our in-situ data show, the SET stress can reactivate an on/off mechanism allowing an over-pressured segment of a fault or a fracture to initiate pore-pressure propagation to adjacent segments. A mechanical reactivation of the adjacent segments becomes plausible (Matthai and Fischer, 1996) due to the important decrease in normal effective stress (Fan et al., 2016; Tobin and Saffer, 2009). Therefore, it becomes possible that a small pressure perturbation promotes earthquakes by the release, thanks to an on/off mechanism, of highly over-pressured fluid along a fault.

Acknowledgments

This work benefited from the support of the BLAME project (ANR-18-CE01-0007; https://anr.fr/Project-ANR-18-CE01-0007) supported by Agence Nationale de la Recherche.

References

Ballas, G., Garziglia, S., Sultan, N., Pelleter, E., Toucanne, S., Marsset, T., Riboulot, V., and Ker, S., 2018, Influence of early diagenesis on geotechnical properties of clay sediments (Romania, Black Sea): Engineering Geology, v. 240, p. 175-188.

Beeler, N. M., and Lockner, D. A., 2003, Why earthquakes correlate weakly with the solid Earth tides: Effects of periodic stress on the rate and probability of earthquake occurrence: Journal of Geophysical Research: Solid Earth, v. 108, no. B8.

Brace, W. F., 1960, An extension of the Griffith theory of fracture to rocks: Journal of Geophysical Research, v. 65, no. 10, p. 3477-3480.

Burns, S. E., and Mayne, P. W., 2002, Analytical cavity expansion-critical state model for piezocone dissipation in fine-grained soils: Soils and Foundations, v. 42, no. 2, p. 131-137.

Cochran, E. S., Vidale, J. E., and Tanaka, S., 2004, Earth tides can trigger shallow thrust fault earthquakes: Science, v. 306, no. 5699, p. 1164-1166.

Crutchley, G. J., Berndt, C., Geiger, S., Klaeschen, D., Papenberg, C., Klaucke, I., Hornbach, M. J., Bangs, N. L. B., and Maier, C., 2013, Drivers of focused fluid flow and methane seepage at south Hydrate Ridge, offshore Oregon, USA: Geology, v. 41, no. 5, p. 551-554.

Dzurisin, D., 1980, Influence of fortnightly Earth tides at Kilauea volcano, Hawaii: Geophysical Research Letters, v. 7, no. 11, p. 925-928.

Elkhoury, J. E., Brodsky, E. E., and Agnew, D. C., 2006, Seismic waves increase permeability: nature, v. 441, no. 7097, p. 1135-1138.

Fan, Z., Eichhubl, P., and Gale, J. F. W., 2016, Geomechanical analysis of fluid injection and seismic fault slip for the Mw4. 8 Timpson, Texas, earthquake sequence: Journal of Geophysical Research: Solid Earth, v. 121, no. 4, p. 2798-2812.

Heaton, T. H., 1982, Tidal triggering of earthquakes: Bulletin of the Seismological Society of America, v. 72, no. 6A, p. 2181-2200.

Holmes, T. R. H., Drusch, M., Wigneron, J. P., and de Jeu, R. A. M., 2008, A global simulation of microwave emission: Error structures based on output from ECMWF's operational integrated forecast system: Ieee Transactions on Geoscience and Remote Sensing, v. 46, no. 3, p. 846-856.

Hurwitz, S., Sohn, R. A., Luttrell, K., and Manga, M., 2014, Triggering and modulation of geyser eruptions in Yellowstone National Park by earthquakes, earth tides, and weather: Journal of Geophysical Research: Solid Earth, v. 119, no. 3, p. 1718-1737.

Ide, S., Yabe, S., and Tanaka, Y., 2016, Earthquake potential revealed by tidal influence on earthquake size–frequency statistics: Nature Geoscience, v. 9, no. 11, p. 834-837.

Judd, A. G., 2003, The global importance and context of methane escape from the seabed: Geo-Marine Letters, v. 23, no. 3, p. 147-154.

Kennel, J., Parker, B., and Hans-Georg, W., 2021, Package ‘earthtide’.

Ker, S., Thomas, Y., Riboulot, V., Sultan, N., Bernard, C., Scalabrin, C., Ion, G., and Marsset, B., 2019, Anomalously deep BSR related to a transient state of the gas hydrate system in the western Black Sea: Geochemistry, Geophysics, Geosystems, v. 20, no. 1, p. 442-459.

Konno, Y., Jin, Y., Yoneda, J., Uchiumi, T., Shinjou, K., and Nagao, J., 2016, Hydraulic fracturing in methane-hydrate-bearing sand: RSC advances, v. 6, no. 77, p. 73148-73155.

Marcon, Y., Römer, M., Scherwath, M., Riedel, M., Dølven, K. O., and Heesemann, M., 2022, Variability of Marine Methane Bubble Emissions on the Clayoquot Slope, Offshore Vancouver Island, Between 2017 and 2021: Frontiers in Earth Science, v. 10, p. Art-Nr.

Matthai, S. K., and Fischer, G., 1996, Quantitative modeling of fault-fluid-discharge and fault-dilation-induced fluid-pressure variations in the seismogenic zone: Geology, v. 24, no. 2, p. 183-186.

Riboulot, V., Cattaneo, A., Scalabrin, C., Gaillot, A., Jouet, G., Ballas, G., Marsset, T., Garziglia, S., and Ker, S., 2017, Control of the geomorphology and gas hydrate extent on widespread gas emissions offshore Romania: BSGF-Earth Sciences Bulletin, v. 188, no. 4, p. 26.

Riboulot, V., Dupre, S., Ker, S., and Sultan, N., 2021, Ghass2 cruise report - doi 10.17600/18001358: Ifremer.

Riboulot, V., Ker, S., Sultan, N., Thomas, Y., Marsset, B., Scalabrin, C., Ruffine, L., Boulart, C., and Ion, G., 2018, Freshwater lake to salt-water sea causing widespread hydrate dissociation in the Black Sea: Nature Communications, v. 9.

Riedel, M., Freudenthal, T., Bergenthal, M., Haeckel, M., Wallmann, K., Spangenberg, E., Bialas, J., and Bohrmann, G., 2020, Physical properties and core-log seismic integration from drilling at the Danube deep-sea fan, Black Sea: Marine and Petroleum Geology, v. 114, p. 104192.

Riedel, M., Hähnel, L., Bialas, J., Bachmann, A. K., Gaide, S., Wintersteller, P., Klaucke, I., and Bohrmann, G., 2021, Controls on gas emission distribution on the continental slope of the western Black Sea: Frontiers in Earth Science, v. 8, p. 601254.

Sano, O., Ito, H., Hirata, A., and Mizuta, Y., 2005, Review of methods of measuring stress and its variations: Bull. Earthq. Res. Inst. Univ. Tokyo, v. 80, p. 87-103.

Sultan, N., Bohrmann, G., Ruffine, L., Pape, T., Riboulot, V., Colliat, J. L., De Prunele, A., Dennielou, B., Garziglia, S., Himmler, T., Marsset, T., Peters, C. A., Rabiu, A., and Wei, J., 2014, Pockmark formation and evolution in deep water Nigeria: Rapid hydrate growth versus slow hydrate dissolution: Journal of Geophysical Research-Solid Earth, v. 119, no. 4, p. 2679-2694.

Sultan, N., Garziglia, S., and Ruffine, L., 2016, New insights into the transport processes controlling the sulfate-methane-transition-zone near methane vents: Scientific Reports, v. 6.

Sultan, N., Plaza-Faverola, A., Vadakkepuliyambatta, S., Buenz, S., and Knies, J., 2020, Impact of tides and sea-level on deep-sea Arctic methane emissions: Nature communications, v. 11, no. 1, p. 1-10.

Tobin, H. J., and Saffer, D. M., 2009, Elevated fluid pressure and extreme mechanical weakness of a plate boundary thrust, Nankai Trough subduction zone: Geology, v. 37, no. 8, p. 679-682.

Woodcock, N. H., Dickson, J. A. D., and Tarasewicz, J. P. T., 2007, Transient permeability and reseal hardening in fault zones: evidence from dilation breccia textures: Geological Society, London, Special Publications, v. 270, no. 1, p. 43-53.

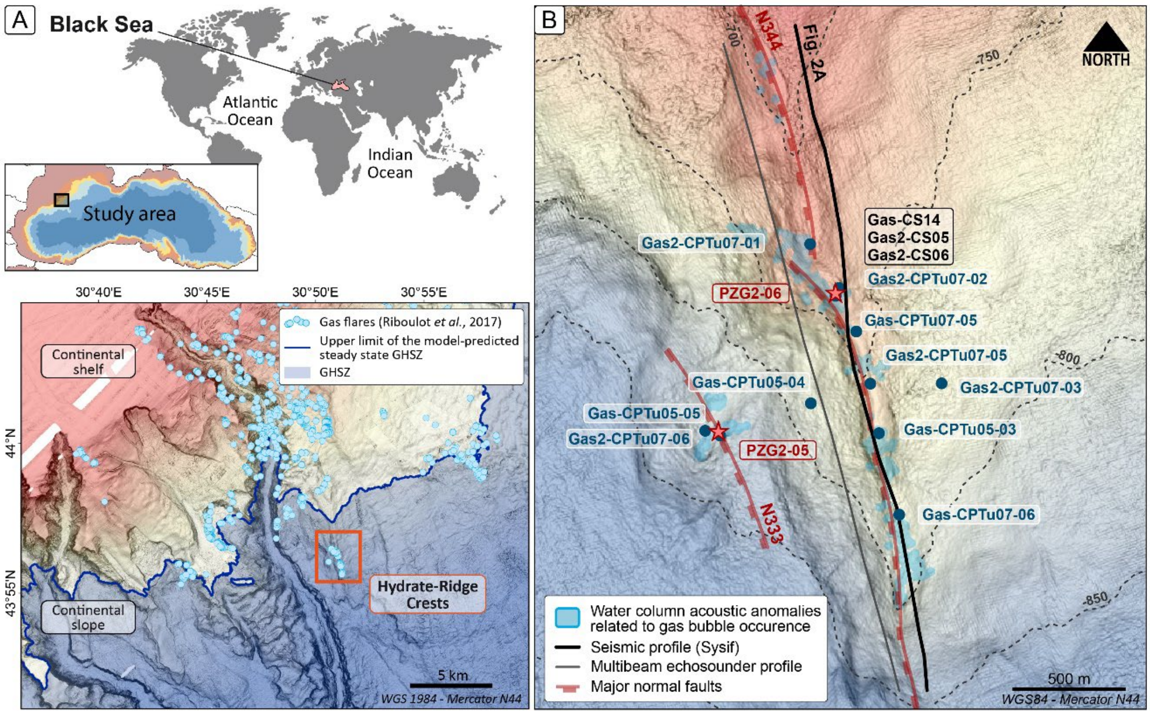

Figure 1. (A) Bathymetric map showing the predicted GHSZ deeper than 660 mbsl and the seepage activity detected in 2015 (Riboulot et al., 2017). (B) Bathymetric map of the HRC with the location of the seismic profile presented in Fig. 2.

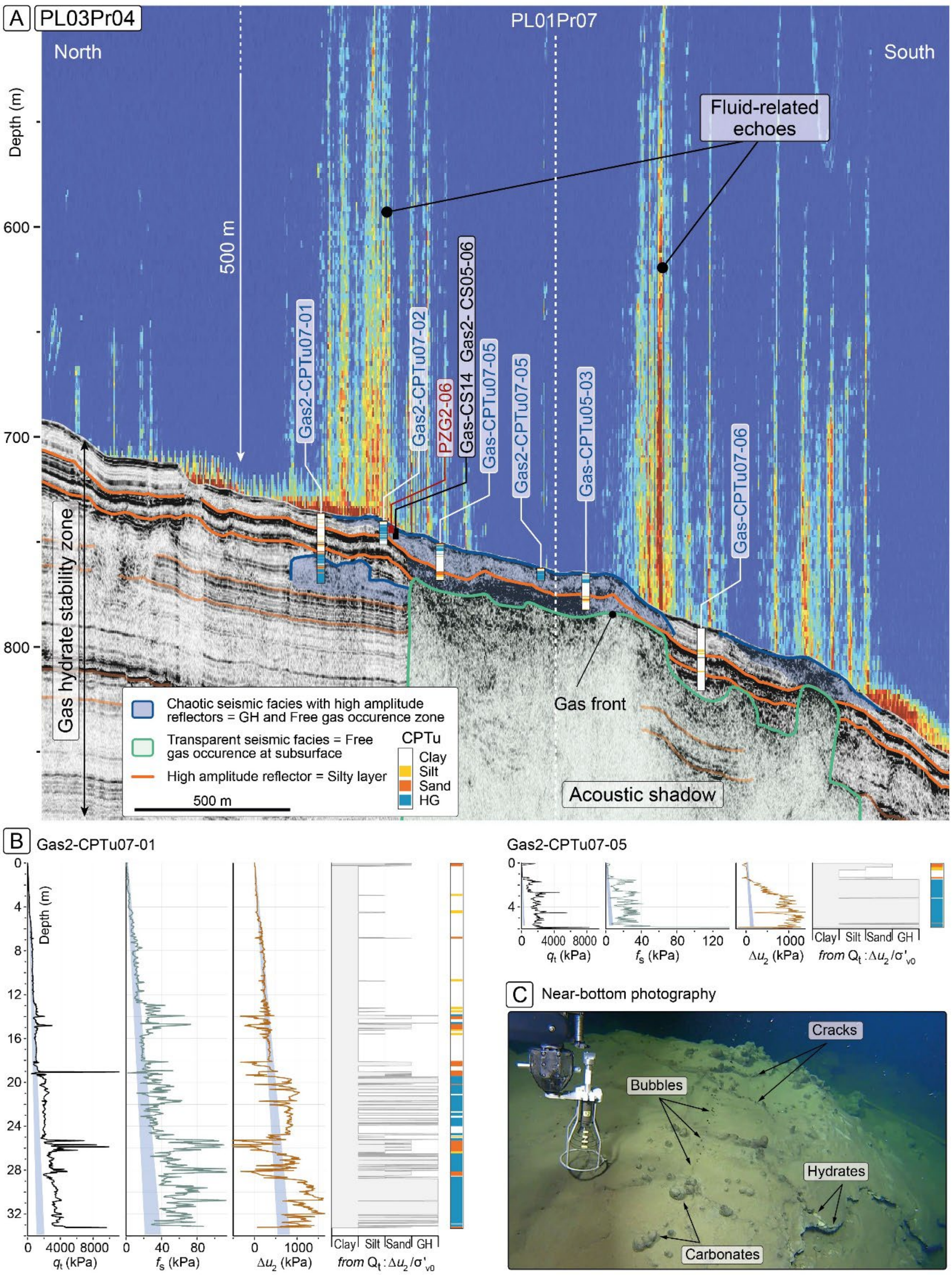

Figure 2. (A) VHR seismic reflection profile PL03PR4 acquired along the main fault track with its interpretation correlate with the in-situ piezocone soundings (CPTu). Acoustic signatures of the water column are superimposed on this seismic profile. The multibeam data are displayed as longitudinal sections with maximum water-column amplitudes, 350 m on both sides of the navigation path along the ~N-S- oriented profile PL03PR04. (B) Two examples of cone penetration tests with pore pressure measurements (CPTu). Piezocones provided continuous vertical readings of cone tip resistance (q_t), sleeve friction (f_s), and penetration pore pressure (Δu_2). (C) Near-bottom photography at the Hydrate Ridge crest (720 m water depth) taken the 14/08/2021 aboard the Nautile submersible during GHASS2 marine expedition

(Riboulot et al., 2021). The picture shows escaping gas bubbles, gas-hydrate interbedded with sediments, small-scale chimneys of methane-derived authigenic carbonates and a fractured seafloor with several conjugate cracks.

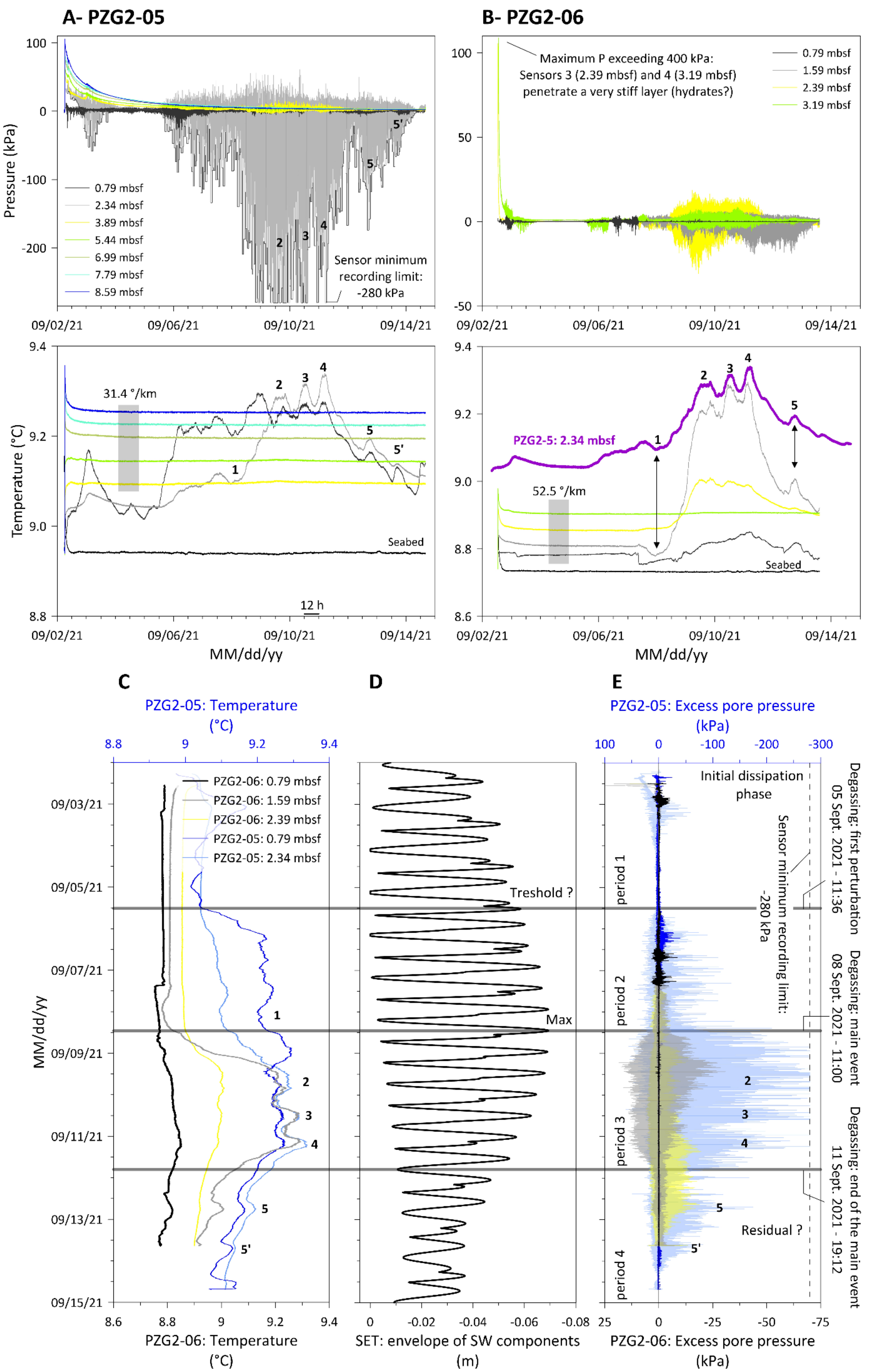

A- PZG2-05
B- PZG2-06
Pressure (kPa)
0.79 mbsf
2.34 mbsf
3.89 mbsf
5.44 mbsf
6.99 mbsf
7.79 mbsf
8.59 mbsf
Sensor minimum recording limit: -280 kPa
Maximum P exceeding 400 kPa: Sensors 3 (2.39 mbsf) and 4 (3.19 mbsf) penetrate a very stiff layer (hydrates?)
1.59 mbsf
2.39 mbsf
3.19 mbsf
Temperature (°C)
31.4 °/km
52.5 °/km
PZG2-5: 2.34 mbsf
Seabed
12 h
MM/dd/yy
C
D
E
PZG2-05: Temperature (°C)
PZG2-06: 0.79 mbsf
PZG2-06: 1.59 mbsf
PZG2-06: 2.39 mbsf
PZG2-05: 0.79 mbsf
PZG2-05: 2.34 mbsf
PZG2-06: Temperature (°C)
Treshold ?
Max
SET: envelope of SW components (m)
PZG2-05: Excess pore pressure (kPa)
PZG2-06: Excess pore pressure (kPa)
Initial dissipation phase
Sensor minimum recording limit: -280 kPa
period 1
period 2
period 3
period 4
Residual ?
Degassing: first perturbation 05 Sept. 2021 - 11:36
Degassing: main event 08 Sept. 2021 - 11:00
Degassing: end of the main event 11 Sept. 2021 - 19:12

283

Figure 3. Piezometer data from (A) site PZG2-05 and (B) site PZG2-06. The temperature time-series data from PZG2-05 recorded at 2.34 mbsf superimposed on the temperature time-series data from PZG2-06 indicate the occurrence during the monitoring period of at least five different concomitant events (numbered from 1 to 5). (C) Temperature versus time from PZG2-05 (2 sensors) and PZG06 (3 sensors) showing the five main events (1 to 5) observed by both piezometers. (D) Envelope of the SW component of the SET versus time and (E) Excess pore pressure (Δu) versus time from PZG2-05 (2 sensors) and PZG06 (3 sensors).

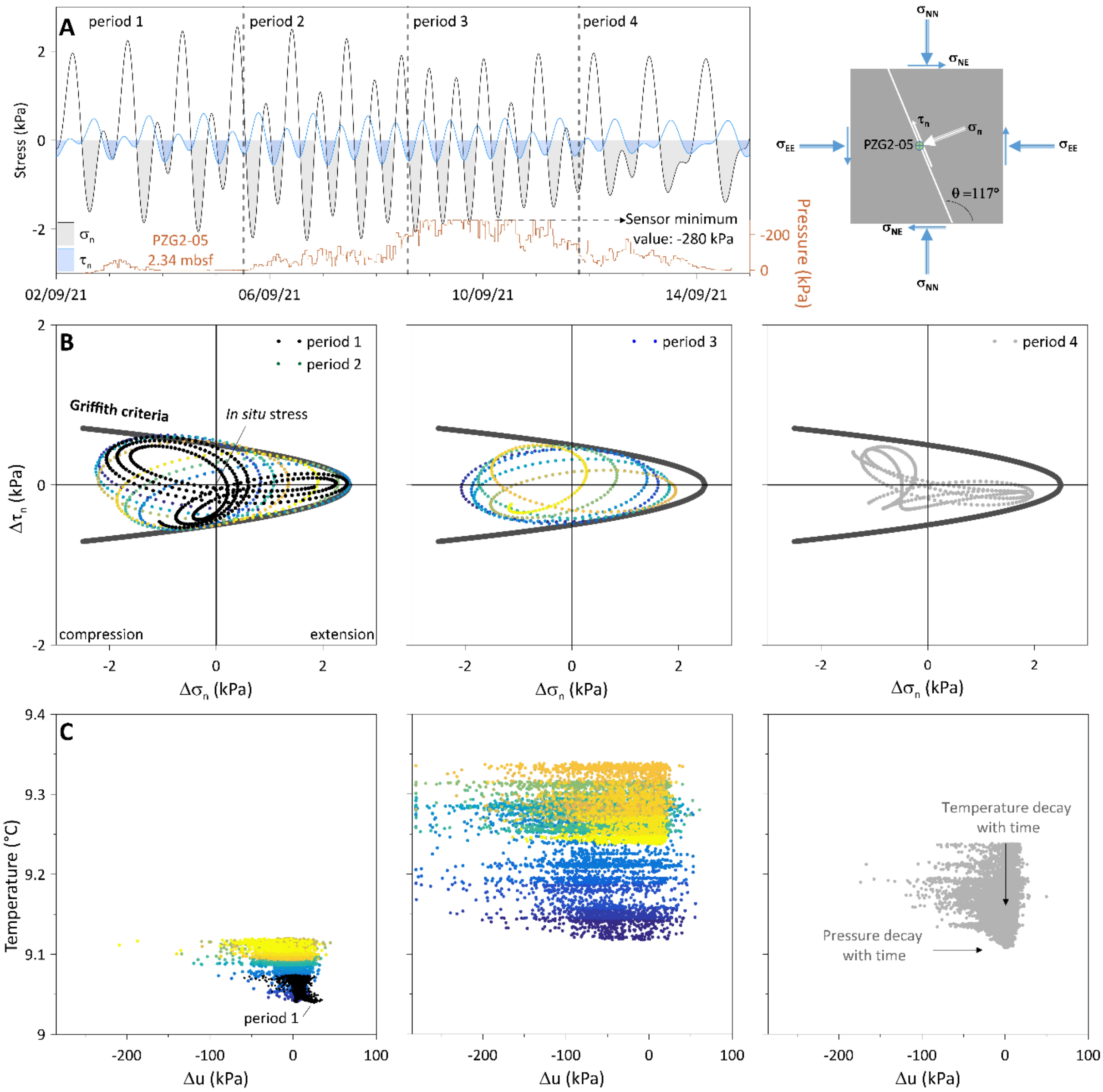

Figure 4. (A) Normal (σ_n) and shear (τ_n) stresses at PZG2-05 site. The shear and normal stresses on the fault plane are shown in the right-hand diagram in (A). The envelope of the negative pore pressure measured by PZG2-05 at 2.34 mbsf is added to the plot. (B) Normal and shear stresses along the fault underlying PZG2-05 plotted in three different Griffith–Coulomb diagrams corresponding to the four different periods. (C) Temperature versus *Δu* from PZG2-05 (2.34 mbsf) for the four different periods. The color in (B) and (B) reflects the time (from dark blue to yellow). Data from period 1 are added to period 2 (black dots).

Supplementary Materials for

Earth tides can reactivate shallow faults and trigger seabed methane emissions

N. Sultan[1], V. Riboulot[1], S. Dupré[1], S. Garziglia[1], S. Ker[1]
[1] Geo-Ocean UMR6538, Ifremer, 29280 Plouzané, France

This PDF file includes:

- Supplementary Text
- Supplementary Figures: Fig. S1 to S9
- Supplementary Tables: Tables S1 to S2

Methods

Acquired data

Seabed and water column data

Ship-borne multibeam surveys were conducted in the HRC area (Riboulot et al., 2021) with the use of a Reson 7150 echosounder. The emitted frequency of 24 kHz at these water depth ranges (600-1000 m) provides a bathymetry map with a resolution of 5 m. In addition to seafloor cartography, multibeam acquisition provided seawater backscatter data. These data are crucial for identifying any target that presents an impedance contrast with surrounding seawater, in particular gas bubbles (Medwin and Clay, 1998) emitted from seeps at continental margins (Dupre et al., 2015; Dupré et al., 2020). The gas emission distribution in Fig. 1B corresponds to the processing and interpretation of 49 multibeam profiles (60-km-long profiles acquired in ~7 h and corresponding to ~18 000 pings) providing full insonification of the hydrate ridge area, including the surroundings of the piezometers (PZG2-05 and PZG2-06). Multibeam data processing was performed with SonarScope and Globe software (Poncelet et al., 2019).

Subseabed seismic data

We used VHR deep-towed multichannel seismic data to investigate the surficial sedimentary column in sufficient detail (the first 200 meters below the seafloor) at around 800 m water depth. The two profiles acquired during the GHASS cruise (Ker et al., 2015) with Ifremer seismic equipment (SYstème SIsmique de Fond, SYSIF) are parallel (Fig. 2A) and perpendicular (Fig. S1) to the main fault track. SYSIF is composed of a Janus-Helmholtz acoustic source (220–1050 Hz) and a 52-channel streamer with a maximum offset of 110 m, tailored for working in high-hydrostatic pressure environments (Ker et al., 2010; Marsset et al., 2014). Recent developments based on wave-equation datuming allowed for fine-scale velocity analysis on SYSIF seismic data sets down to 50-100 m below seafloor (Colin et al., 2020). Seismic resolution of the SYSIF profiles PL03PR04 (Fig. 2A) and PL01PR07 (Fig. S2) is less than 1 m vertically and 3 m horizontally.

Piezometer

The piezometer is designed to measure in-situ excess pore pressure (i.e., above hydrostatic) and temperature. In-situ excess pore pressure and temperature measurements were made using a cable-deployed piezometer equipped with a sediment lance of 60 mm diameter carrying differential pore pressure (pore pressures in excess of hydrostatic pressures or excess pore pressure) and temperature sensors, ballasted with lead weights (up to 1000 kg). The piezometer pore pressure and temperature sensors have an accuracy of ±0.5 kPa and 0.05 °C, respectively. The length of the piezometer lance (9.07 m for PZG2-05 and 3.67 m for PZG2-06 – Table S1) was adapted to the studied site and the expected stiffness of sediment with mainly the presence of soft sediments at site PZG2-05 and shallow massive hydrate at site PZG2-06 (Fig. 2B and fig. S1). The thermal gradients at PZG2-05 and PZG2-06 are derived from the sensors showing a stable signal after the piezometer deployments (Fig. S2 and Fig. S3).

Penfeld piezocone and Vp

Cone penetration testing with pore pressure measurements (CPTu) were carried out with pressure-compensated piezocones pushed into sediment with the Penfeld penetrometer during the GHASS (Ker et al., 2015) and GHASS2 (Riboulot et al., 2021) cruises. Piezocones provided continuous vertical readings of cone-tip resistance (*qt*), sleeve friction (*fs*), and penetration pore pressure (Δu_2). Following the approach proposed by Schneider and co-authors (Schneider et al., 2008) the contrasted responses of clay, silt and sand sediments during piezocone penetration were used to obtain detailed continuous stratigraphic profiles (Fig. 2B and Fig. S1). The determination of stratigraphy was refined by considering the criteria to detect the presence of GHs in clayey sediments from simultaneous increases in piezocone readings above the trends commonly exhibited by their hydrate-free counterparts (Taleb et al., 2018). These trends were derived from the combined analyses of sediment cores and piezocone data carried out by Ballas and co-authors (Ballas et al., 2018) in the vicinity of the study area. Accordingly, a simple algorithm was developed (equation 1) to automatically detect the presence of GHs in clayey sediments.

$$\begin{aligned} q_t\,(kPa) &> 58\,z + 70 \\ f_s\,(kPa) &> 1.1\,z + 2 \\ \Delta_{u2}\ (kPa) &> 24\,z + 20 \end{aligned} \qquad (1)$$

where *z* is depth in meters below seafloor

A sonic fork was used to measure the in-situ P-wave velocity (Vp). As for the CPTu measurements, the Vp fork is pushed into sediment with the Penfeld penetrometer. The sonic fork measures every 2 cm by producing a 1-MHz compressional wave and the amplitude ratio between the input and received signals provides attenuation (Taleb et al., 2018). Thanks to this sonic fork, it is possible to detect hydrate-bearing sediments (high Vp values, often > 1800 m/s), gassy sediments (low Vp values, often < 1000 m/s) and sedimentary layers with the coexistence of free gas and GHs (alternating low and high Vp values) (Fig. 1B).

Calculations

Generation of synthetic Earth Tides

Ocean tides and the SET are determined using the EarthTide-package (Kennel et al., 2021) based on the R (Team, 2013) programming language. The EarthTide-package is a parallel implementation of the Earth tide software ETERNA 3.40 (Wenzel, 1996a). The synthetic Earth tide data are obtained for a given date and location.

Fig. S4A and Fig. S4B shows the NS and EW displacements of the SET indicating a phase shift between the two components. Fig. S4B shows the two in-phase behaviors between the SET vertical displacement and the ocean tides. One of the positive peaks of the vertical SET underlined by a vertical arrow in Fig. S4B was added to Fig. S4A to illustrate the phase shift between the three components of the SET. The NS displacement of the SET was also calculated for the five-month period preceding piezometer deployment. Fig. S4C indicates that a period of around 135 days separates the peak recorded during piezometer deployment from a previous peak of comparable magnitude. It is important to note that the phase shift between the main SET displacement components (Fig. S5) prevents any direct spectral correlation analysis between the SET data and piezometer records. Indeed, piezometer data are expected to be affected by the 3D-dephased-SET perturbations.

Strain induced by SET perturbations

For a SET displacement vector (u_r, u_θ, u_ϕ) in spherical coordinates (r, θ, ϕ) and under small deformations, the components of the strain tensor are given in Fig. S6 and equations 2 to 7.

$$\varepsilon_{rr} = \varepsilon_{ZZ} = \frac{\partial u_r}{\partial r} \tag{2}$$

$$\varepsilon_{\theta\theta} = \varepsilon_{NN} = \frac{1}{r}\left(\frac{\partial u_\theta}{\partial \theta} + u_r\right) \tag{3}$$

$$\varepsilon_{\phi\phi} = \varepsilon_{EE} = \frac{1}{r\,\sin\theta}\left(\frac{\partial u_\phi}{\partial \phi} + u_r\,\sin\theta + u_\theta\,\cos\theta\right) \tag{4}$$

$$\varepsilon_{r\theta} = \varepsilon_{ZN} = \frac{1}{2}\left(\frac{1}{r}\frac{\partial u_r}{\partial \theta} + \frac{\partial u_\theta}{\partial r} - \frac{u_\theta}{r}\right) \tag{5}$$

$$\varepsilon_{\theta\phi} = \varepsilon_{NE} = \frac{1}{2r}\left(\frac{1}{\sin\theta}\frac{\partial u_\theta}{\partial \phi} + \frac{\partial u_\phi}{\partial \theta} - u_\phi\,\cot\theta\right) \tag{6}$$

$$\varepsilon_{\phi r} = \varepsilon_{EZ} = \frac{1}{2}\left(\frac{1}{\mathrm{r}\,\sin\theta}\frac{\partial u_r}{\partial \phi} + \frac{\partial u_\phi}{\partial r} - \frac{u_\phi}{r}\right) \tag{7}$$

Stress induced by SET perturbations

The relationship between stresses and strains for an isotropic elastic material is given by the following constitutive equation:

$$\boldsymbol{\sigma} = 2\mu\boldsymbol{\epsilon} + \lambda tr(\boldsymbol{\varepsilon})\mathbf{I} \tag{8}$$

where **σ** and **ε** are respectively the stress and strain tensor, **I** the identity matrix and *tr* the trace function. λ and μ are Lamé's constants.

Equations 2 to 8 clearly show that the stress along a given direction does not depend only on the displacement along this same direction (Emter, 1997). Moreover, the stress applied on a geological structure is affected by the geometric characteristics of the structure.

For shallow geological structures (< 200 km), the radial stress component can be neglected (Varga and Grafarend, 2019). The stress-strain relationship can thus be analyzed in a 2D plane (latitude-longitude). Therefore, for $\sigma_{NN} > \sigma_{EE}$, the normal stress σ_n and the shear stress τ_n acting on any plane, making an angle α with the horizontal (fig. 6b), can be determined by using equations 9 and 10.

$$\sigma_n = \frac{\sigma_{NN}+\sigma_{EE}}{2} + \frac{\sigma_{NN}-\sigma_{EE}}{2}\cos 2\alpha + \sigma_{NE}\sin 2\alpha \tag{9}$$

$$\tau_n = \frac{\sigma_{NN}-\sigma_{EE}}{2}\sin 2\alpha - \sigma_{NE}\cos 2\alpha \tag{10}$$

The strain tensor generated by the SET is calculated using equations 2 to 8 (Kennel et al., 2021). Under the hypothesis of isotropic elastic Earth undergoing small deformations, an elastic constitutive law (equation 8) can be used to derive the 3D stress tensor. Lamé's constants (λ and μ) are considered equal to 32 GPa (Matsumoto et al., 2001). The high values of Lamé's constants are usually used for stiff rocks but the presence of massive GHs and the depth of the free gas below the BSR, which is expected to be one of the main reservoirs feeding the degassing phenomenon, justify their use. Equations 8 and 9 are used to determine the normal (σ_n) and shear (τ_n) stresses generated by the SET on the two main faults underlying PZG2-05 and PZG2-06 (Fig. 4 and Fig. S7). These faults are N344 (PZG2-06) and N333 (PZG02-05) oriented (respectively 106° and 117° anticlockwise from the horizontal). It should be noted that the stress tensor is calculated in the field of linear elasticity where the superposition principle is valid. Therefore, for changed values of Lamé's constants, one may expect a change in the stress tensor values but not in the tendency of the plots shown in Fig. 6b.

Acoustic data

Water-column acoustic data recorded in the hydrate ridge area in 2015 (Ker et al., 2015) and 2021 (Riboulot et al., 2021) were investigated to i) address and characterize the spatio-temporal variability of gas emissions from the seafloor into the water column (Fig. S1) and ii) check if this variability is related to SET cycles (Fig. S8 and Fig. S9). Both datasets were acquired aboard the research vessel Pourquoi pas? with a Reson 7150 ship-borne multibeam echosounder. Data analysis focused on comparisons of gas-emission events recorded along similar ship tracks with identical acquisition and survey parameters (i.e., frequency, range, gain, power and pulse length) (Table S2). These conditions are necessary to avoid biases related to insonification geometry (e.g., distance from the transducers to the gas bubbles, incidence angle) and to target only the acoustic variations related to changes in gas bubbling dynamics. To best illustrate this variability, echo-integration maps of the water-column acoustic signal are displayed in Fig. S8 (instead of water-column polar echograms). The amplitude of the acoustic signal is integrated within a horizontal water-column slice (Dupre et al., 2015) similarly to what is performed in fishery acoustics (Dragesund and Olsen, 1965).

Sensor accuracy, calculation uncertainties and inconsistency

The piezometer pore-pressure sensors have an accuracy of ±0.5 kPa. This good sensor accuracy has a negligible effect on the interpretation since, as shown in Fig. 3, the ±0.5 kPa is almost within the thickness of the plot curves. However, the piezometer temperature sensors have an accuracy of 0.05°C, which may affect the calculated depth of the source of the expulsed fluid at sites PZG2-05 and PZG2-06. The vertical depth error lies between ±1 (site PZG2-06) and ±1.5 m (site PZG2-05) and is comparable to the vertical resolution of the SYSIF seismic profiles, which provide the depth of the coarse sediment layers (thick orange reflectors in Fig. 2) considered as the intermediate reservoir of the expulsed fluids. Although it would be interesting to improve this depth error, it should be noted that a higher precision of the depth of these layers would not affect the described process.

Uncertainties concerning the SET calculation are well described by Wenzel (Wenzel, 1996b) who showed that the prediction of SET signals is obtained with an accuracy better than 1 ngal (1 ngal = 0.01 nm/s²). In terms of displacement, this gives, for instance, an accuracy in the order of 2 10^{-4} m for the vertical components, largely suitable for the analysis carried out in this manuscript.

Water-column acoustic records did not confirm the correlation between SET cycles (e.g., N component, Fig. S9) and gas emissions into the water column. Although an increase in gas emissions was observed following a period during which the N component of the SET reaches a maximum (e.g., events 39 and 41 in fig. S1 and fig. S9), spatio-temporal variability of gas emissions was also observed on the contrary in periods of presumably quiescence (e.g., events 1 and 24 in Fig. S8 and Fig. S9). It is worth noting that the number of possible comparisons of acoustic gas events is relatively limited by the discontinuous dataset (i.e., similar acquisition and survey parameters). It becomes therefore more appropriate to focus the interpretation on a continuous time-series data akin to that acquired using the piezometers.

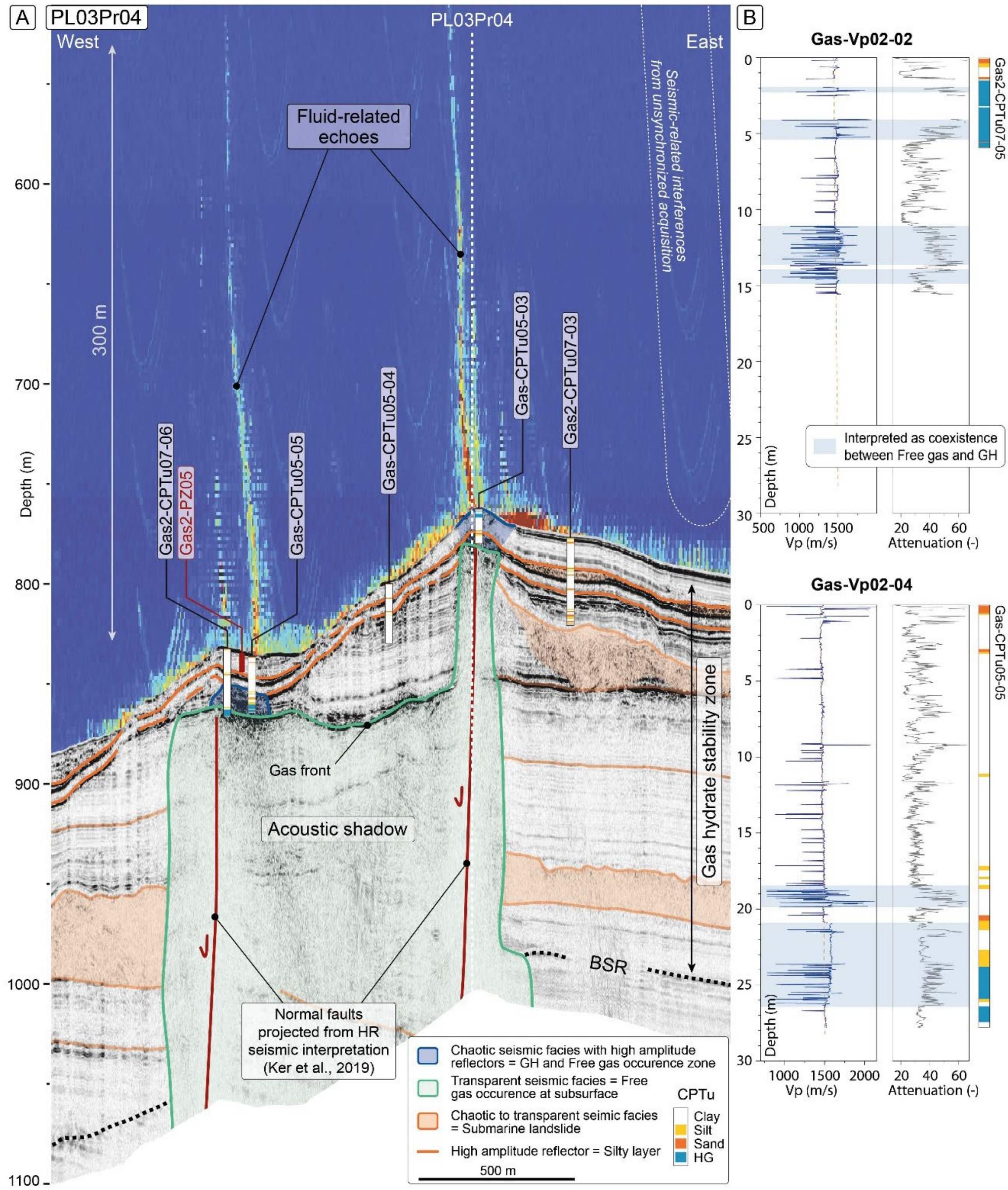

Fig. S1. (A) The VHR seismic reflection profile PL01PR07 crossing the main fault track with its interpretation correlate with the in-situ CPTu and Vp readings confirming the coexistence of free gas and gas hydrates beneath the HRC. Acoustic signatures of the water column are superimposed on this deep-towed seismic profile. The multibeam data are displayed as longitudinal sections with maximum water-column amplitudes, 350 m on both sides of the navigation path. The multi-ping insonification (x4) of the 24 kHz 7150 Reson echosounder allows high-resolution display of the water column with identified echo amplitudes caused by the presence of gas bubbles escaping from the seafloor into the water column. (B) P wave velocity profiles at sites Gas-Vp02-02 and Gas-Vp02-04 showing several intervals (dashed blue) with coexistence of free-gas and gas hydrate.

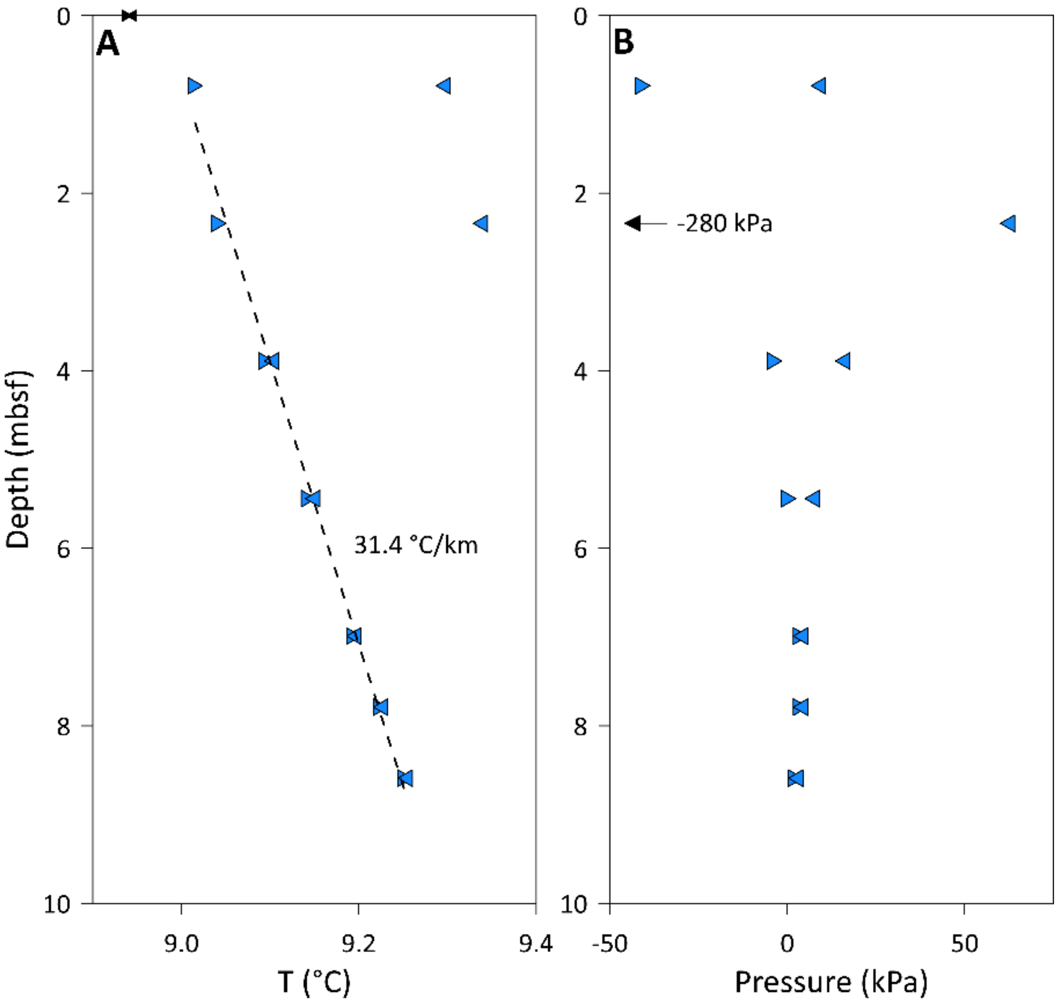

Fig. S2. PZG2-05: (A) temperature and (B) pressure versus depth. The thermal gradient in (A) is determined from the period and the sensor data obtained within the gray areas shown in Fig. 3. Triangles indicate minimum and maximum values during the degassing phase.

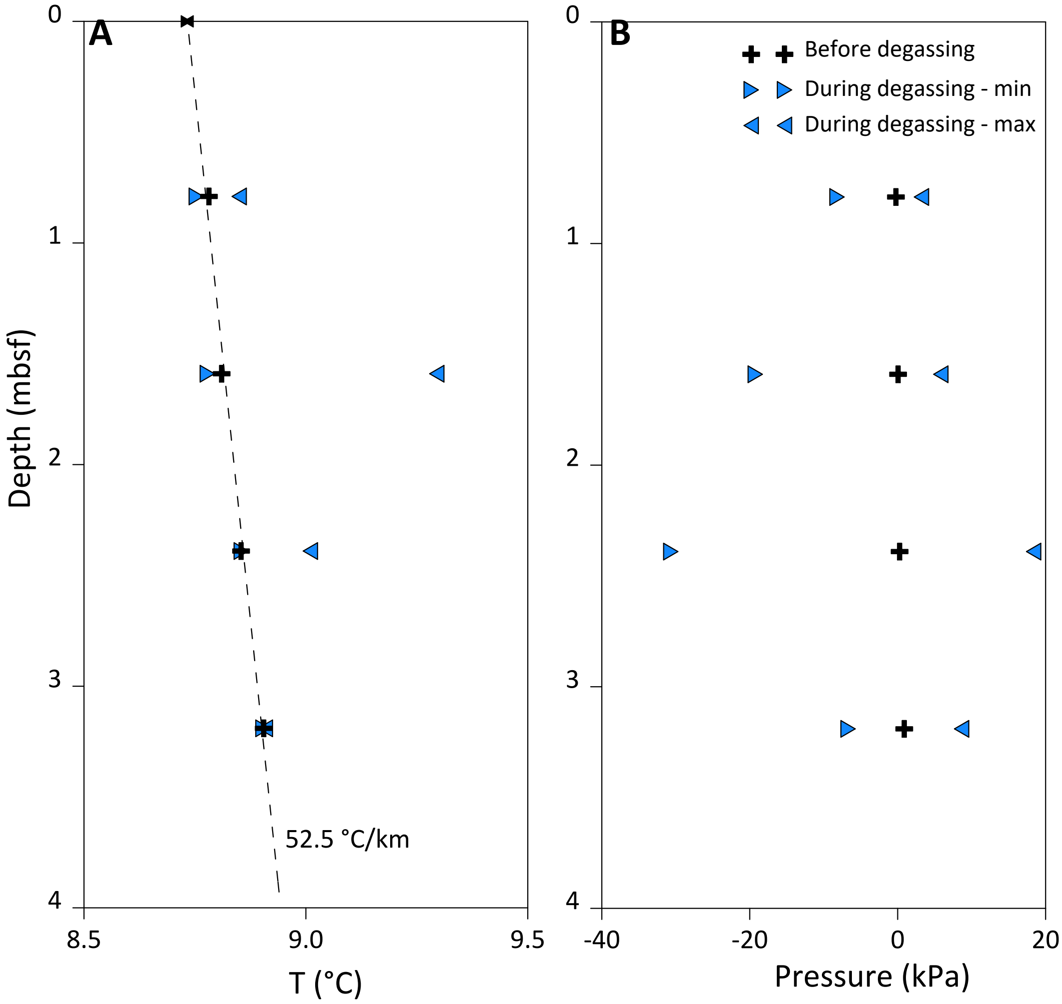

Fig. S3. PZG2-06: (A) temperature and (B) pressure versus depth. The thermal gradient in (A) is determined from the period and the sensor data obtained within the gray areas shown in Fig. 3A and Fig. 3B. Triangles indicate minimum and maximum values during the degassing phase.

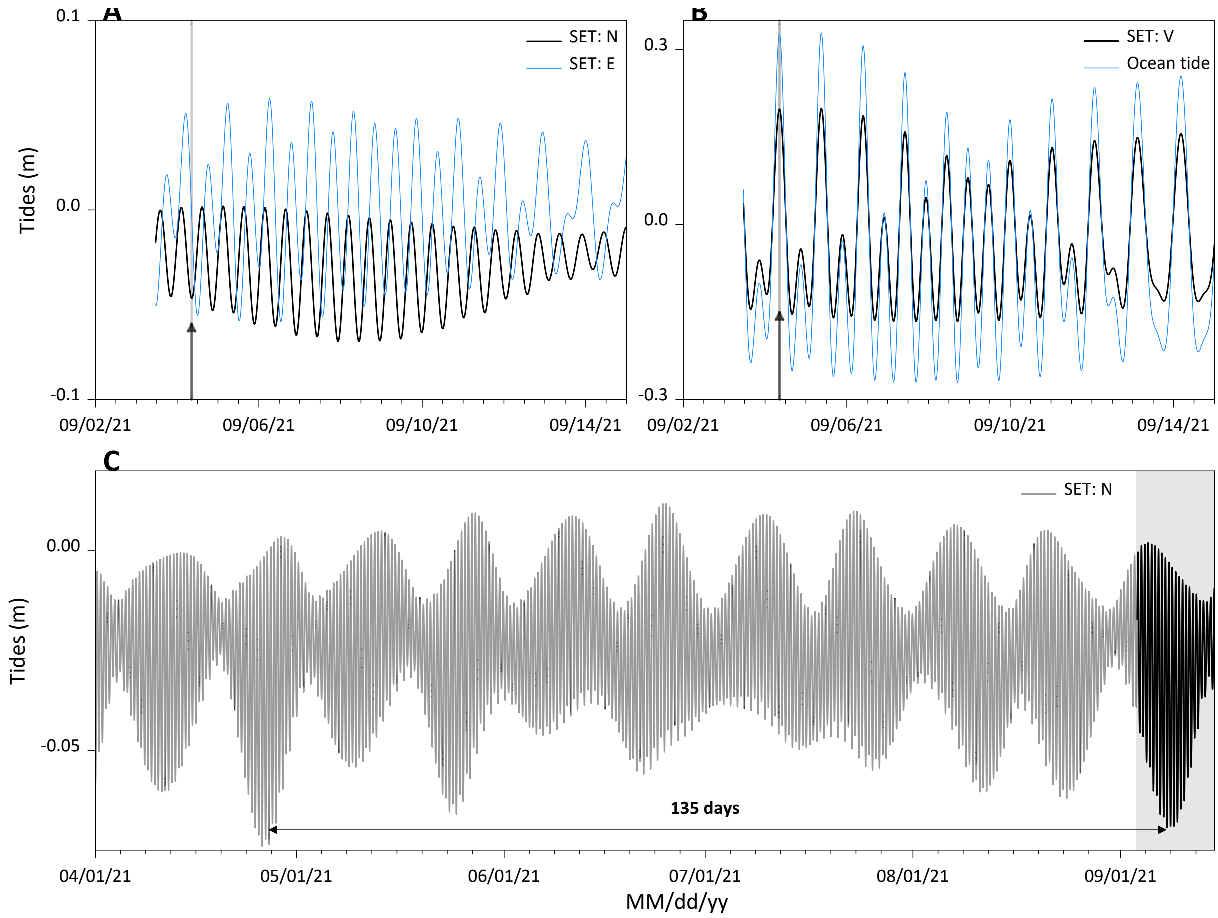

Fig. S4. Ocean tides and solid Earth tides calculated for the Black-Sea hydrate ridge site. (A) NS and EW components of the SET (positive for displacement towards the north and the east). (B) Ocean tides and vertical component of the SET (positive for upward displacement). One of the peaks of the ocean tide and the vertical SET indicated by a vertical arrow in (B) is added to (A) to illustrate the phase shift between the three components of the SET. (C) NS displacement of the SET calculated for the 5-month period preceding piezometer deployment. A period of around 135 days separates the peak recorded during piezometer deployment (gray area) from a previous comparable peak.

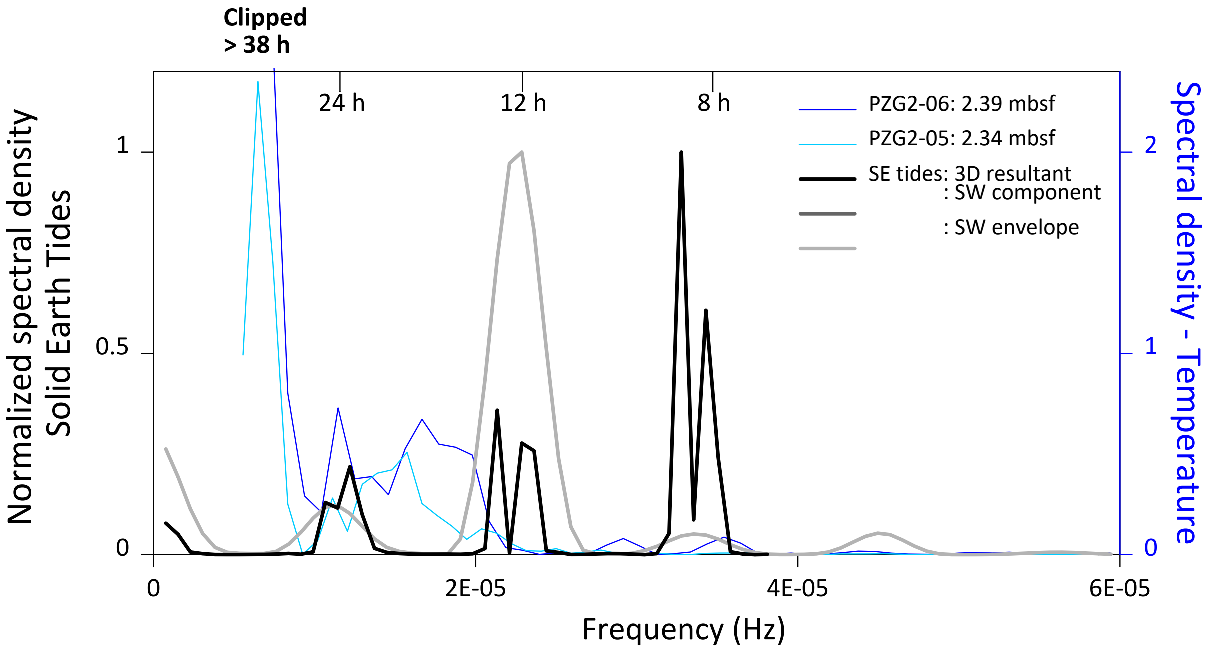

Fig. S5. Spectral analysis of time-series data obtained from PZG2-05 (sensor at 2.34 mbsf), PZG2-06 (sensor at 2.39 mbsf) and the three components of the SET - Diurnal tides (period T = 1 day), Semidiurnal tides (period T = 1/2 day) and Terdiurnal tides (period T = 1/3 day) are indicated.

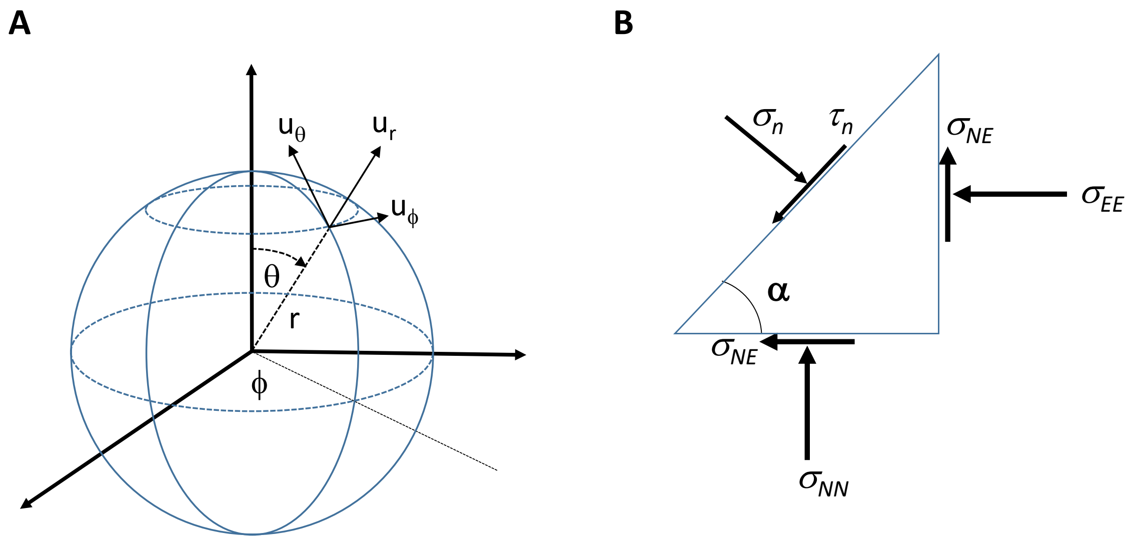

Fig. S6. (A) strain tensor in spherical coordinates. *r* is the radial distance and ϕ and θ are respectively the longitude and latitude. The three components of the displacement vector (u_r, u_θ, u_ϕ) are in the positive direction (upwards, to the east and to the north). (B) Normal (σ_n) and shear (τ_n) stresses on a plane at an angle α to the horizontal plane.

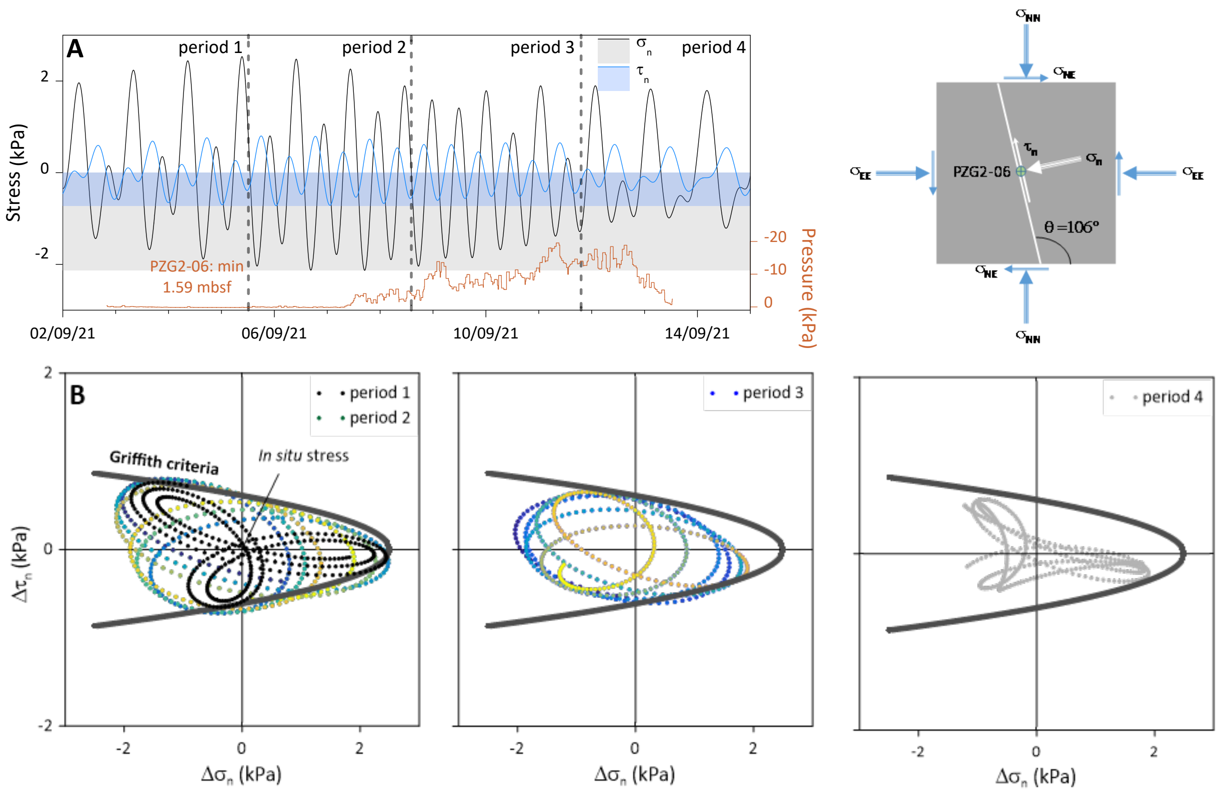

Fig. S7. Normal (σ_n) and shear (τ_n) stresses at site PZG2-06 versus time on the fault creating an angle of 106° with the horizontal (344N). (A) The shear and normal stress vectors on the fault plane are shown in the diagram on the right in (A). The envelope of the negative pore pressure measured by PZG2-06 at 1.59 mbsf is added to the plot. (B) Normal (σ_n) and shear (τ_n) stresses along the fault underlying PZG2-06 plotted in three different Griffith–Coulomb diagrams corresponding to the four different periods. The color in (B) reflects the time (from dark blue to yellow). Data from period 1 are added to period 2 (black dots).

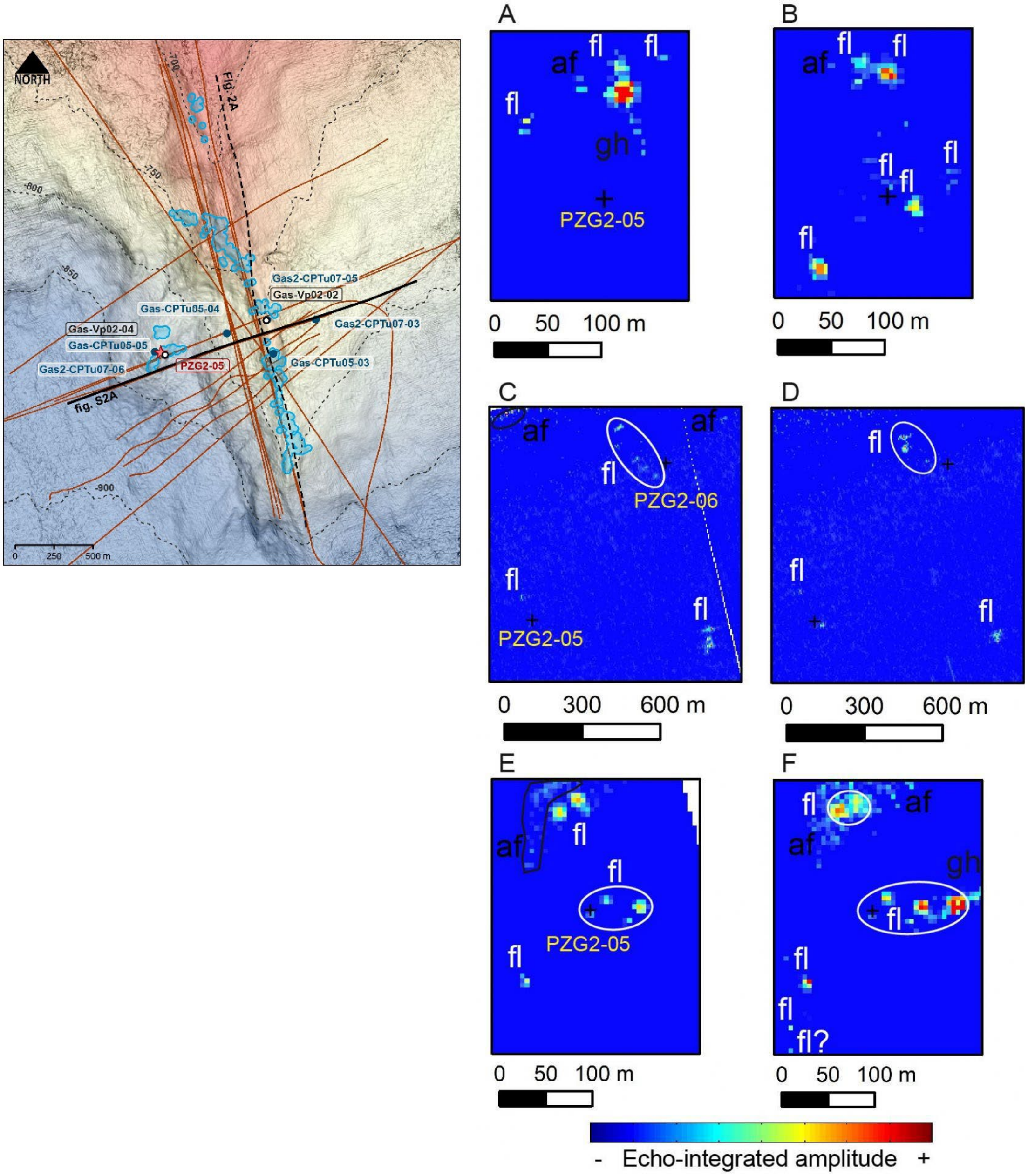

Fig. S8. Water-column echo-integration maps (Dupre et al., 2015) derived from processed polar echograms at the hydrate ridge in the PZG2-05 and PZG2-06 areas (used multibeam profiles diagram on the left) illustrating the spatio-temporal variability of gas emissions. (A, B) yearly basis between 14/09/2015 and 28/08/2021. (C, D) monthly basis between 28/08/2021 and 29/09/2021 and (E, F) hourly basis between 09/09/2021 at 14:58:00 and ~1 hour later. Each couple (A, B), (C, D), (E, F) corresponds to the same insonification area at two indicated different times. fl, gh and af stand for fluid-related echo, ghost of fluid-related echo and artefact-related echo, respectively. The height of the echo-integration slice is set to 10 m for A, B, E and F (with an upper limit at 25 m above the seafloor) and 100 m for C and D (with an upper limit at 300 m above the seafloor). To avoid biases in water-column acoustic response to insonification geometry, only multibeam data profiles with the same acquisition setting were compared with each other (Table S1). The gas-emission events are labelled from A to F as 1, 24, 26-27, 30-31, 39 and 41.

This is a Preprint and has not been peer reviewed

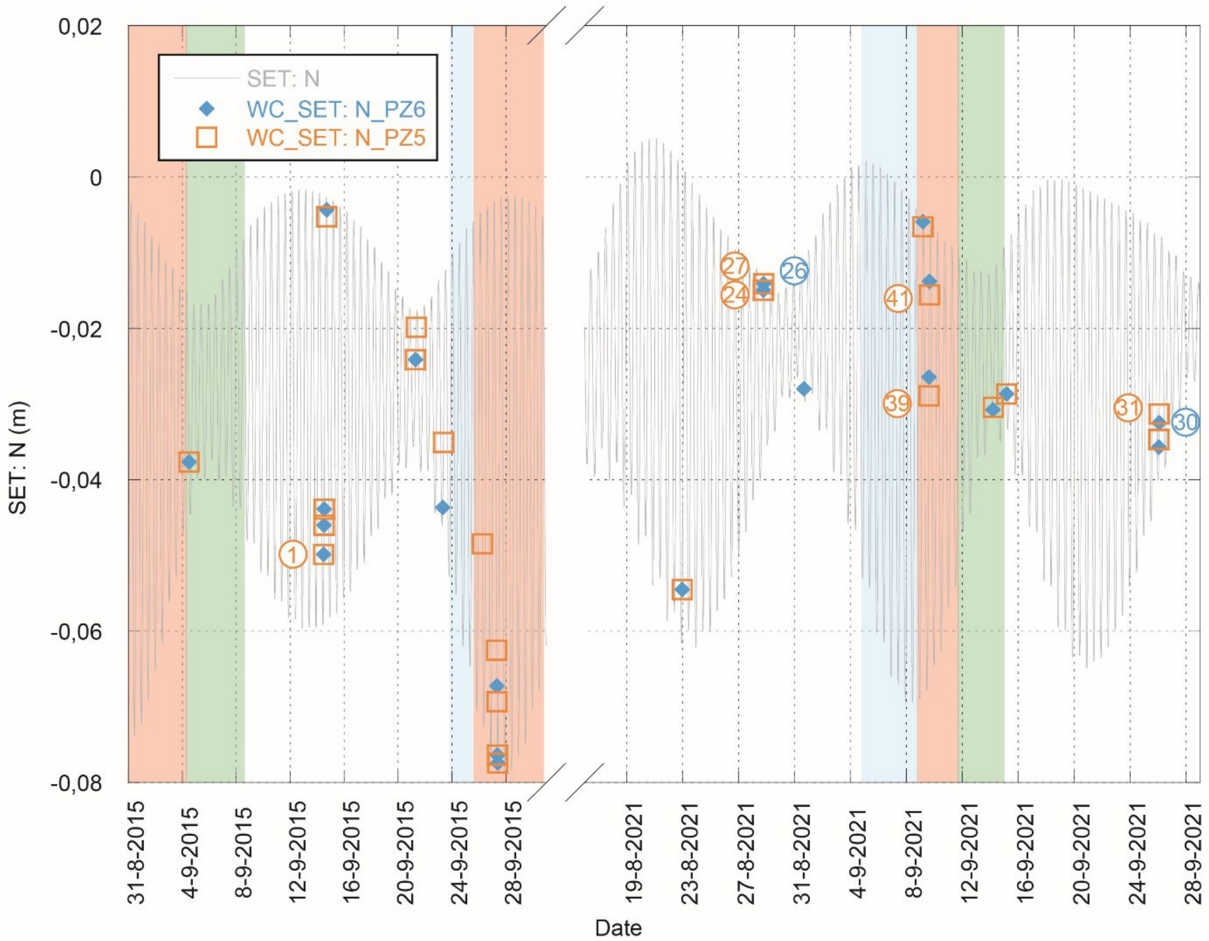

Fig. S9. Predicted SET (N component, Fig. 4A) during GHASS (Ker et al., 2015) and GHASS2 (Riboulot et al., 2021) multibeam surveys with gas-emission events recorded in the vicinity of PZG2-05 and PZG2-06 piezometer deployments (WC_SET). Several multibeam profiles (29), corresponding to 44 main gas events, were thus used to compare the acoustic signatures of escaping gas bubbles between periods of presumed gas-circulation (considering a possible threshold on the N component of ~-0.07) and quiescence periods before and after (blue and green bars). Six of these gas events (1, 24, 26-27, 30-31, 39 and 41, Table S1) and associated comparisons are reported in fig. S1.

Names	# of sensors T: temperature sensor P: pressure sensor	Coordinates	Water depth (m)	Length (m)	Recording period MM/dd/yyyy HH:mm
PZG2-05	8T - 7P	43.9341 - 30.8443	~ 818	9.07	09/02/2021 06:41 - 09/14/2021 16:00
PZG2-06	5T - 4P	43.9395 - 30.8507	~ 732	3.67	09/02/2021 13:05 - 09/13/2021 14:45

Table S1. Piezometer stations. Characteristics of piezometers used in the present study.

File name (date_time)	Gas-emission event number (in Fig. S7)	Number of beams	Main frequency (kHz)	Number of swaths	Angular range (deg)	Interping distance (m)	Heading (deg)	Direction	Ship speed (nd)	Signal length (ms)	Range (m)	Power (dB)	Gain (dB)
20150914_115203	1	880	24.0	1	116	10.8	165	N-S	8.1	3	1600	222	11
20210828_184356	24	880	24.0	1	117	6.5	161	N-S	5.0	3	1600	222	11
20210828_191521	26, 27	880	24.0	1	117	6.8	255	E-W	5.3	3	1600	222	11
20210926_021018	30, 31	880	24.0	1	117	8.1	254	E-W	6.0	3	1600	222	11
20210909_145110	39	880	22.5	4	116	1.3	64	SW-NE	2.2	3	1600	222	11
20210909_155311	41	880	22.5	4	116	1.3	61	SW-NE	2.3	3	1600	222	11

Table S2. Acquisition parameters of multibeam profiles used in Fig. S8.

References

Ballas, G., Garziglia, S., Sultan, N., Pelleter, E., Toucanne, S., Marsset, T., Riboulot, V., and Ker, S., 2018, Influence of early diagenesis on geotechnical properties of clay sediments (Romania, Black Sea): Engineering Geology, v. 240, p. 175-188.

Colin, F., Ker, S., Riboulot, V., and Sultan, N., 2020, Irregular BSR: Evidence of an ongoing reequilibrium of a gas hydrate system: Geophysical Research Letters, v. 47, no. 20, p. e2020GL089906.

Dragesund, O., and Olsen, S., 1965, On the possibility of estimating year-class strength by measuring echo-abundance of 0-group fish.

Dupre, S., Scalabrin, C., Grall, C., Augustin, J.-M., Henry, P., Sengor, A. M. C., Goeruer, N., Cagatay, M. N., and Geli, L., 2015, Tectonic and sedimentary controls on widespread gas emissions in the Sea of Marmara: Results from systematic, shipborne multibeam echo sounder water column imaging: Journal of Geophysical Research-Solid Earth, v. 120, no. 5, p. 2891-2912.

Dupré, S., Loubrieu, B., Pierre, C., Scalabrin, C., Guérin, C., Ehrhold, A., Ogor, A., Gautier, E., Ruffine, L., and Biville, R., 2020, The Aquitaine Shelf edge (Bay of Biscay): A primary outlet for microbial methane release: Geophysical Research Letters, v. 47, no. 7, p. e2019GL084561.

Emter, D., 1997, Tidal triggering of earthquakes and volcanic events, Tidal phenomena, Springer, p. 293-309.

Kennel, J., Parker, B., and Hans-Georg, W., 2021, Package 'earthtide'.

Ker, S., Marsset, B., Garziglia, S., Le Gonidec, Y., Gibert, D., Voisset, M., and Adamy, J., 2010, High-resolution seismic imaging in deep sea from a joint deep-towed/OBH reflection experiment: application to a Mass Transport Complex offshore Nigeria: Geophysical Journal International, v. 182, no. 3, p. 1524-1542.

Ker, S., Riboulot, V., and Team, G. C., 2015, GHASS cruise report doi:10.17600/15000500: Ifremer report.

Marsset, B., Menut, E., Ker, S., Thomas, Y., Regnault, J.-P., Leon, P., Martinossi, H., Artzner, L., Chenot, D., Dentrecolas, S., Spychalski, B., Mellier, G., and Sultan, N., 2014, Deep-towed High Resolution multichannel seismic imaging: Deep-Sea Research Part I-Oceanographic Research Papers, v. 93, p. 83-90.

Matsumoto, K., Sato, T., Takanezawa, T., and Ooe, M., 2001, GOTIC2: A program for computation of oceanic tidal loading effect: Journal of the Geodetic Society of Japan, v. 47, no. 1, p. 243-248.

Medwin, H., and Clay, C. S., 1998, Fundamentals of acoustical oceanography, Elsevier.

Poncelet, C., Billant, G., and Corre, M.-P., 2019, Globe (GLobal Oceanographic Bathymetry Explorer) Software.

Riboulot, V., Dupre, S., Ker, S., and Sultan, N., 2021, Ghass2 cruise report - doi 10.17600/18001358: Ifremer.

Schneider, J. A., Randolph, M. F., Mayne, P. W., and Ramsey, N. R., 2008, Analysis of Factors Influencing Soil Classification Using Normalized Piezocone Tip Resistance and Pore Pressure Parameters: Journal of Geotechnical and Geoenvironmental Engineering, v. 134, no. 11, p. 1569-1586.

Taleb, F., Garziglia, S., and Sultan, N., 2018, Hydromechanical properties of gas hydrate-bearing fine sediments from in situ testing: Journal of Geophysical Research: Solid Earth, v. 123, no. 11, p. 9615-9634.

Team, R. C., 2013, R: A language and environment for statistical computing.

Varga, P., and Grafarend, E., 2019, Influence of tidal forces on the triggering of seismic events, Geodynamics and Earth Tides Observations from Global to Micro Scale, Springer, p. 55-63.

Wenzel, H.-G., 1996a, The nanogal software: Earth tide data processing package ETERNA 3.30: Bull. Inf. Marées Terrestres, v. 124, p. 9425-9439.

Wenzel, H. G., 1996b, Accuracy assessment for tidal potential catalogues: Marées terrestres (Bruxelles), v. 124, p. 9394-9416.